Analytical and Bioanalytical Chemistry
https://doi.org/10.1007/s00216-023-04540-x

RESEARCH PAPER

Quantification of monodisperse and biocompatible gold nanoparticles by single-particle ICP-MS

Alex N. Frickenstein[1] · Shirsha Mukherjee[1] · Tekena Harcourt[1] · Yuxin He[1] · Vinit Sheth[1] · Lin Wang[1] · Zain Malik[1] · Stefan Wilhelm[1,2,3]

Received: 8 December 2022 / Revised: 3 January 2023 / Accepted: 11 January 2023

Abstract

Bioanalytical and biomedical applications often require nanoparticles that exhibit narrow size distributions and biocompatibility. Here, we demonstrate how different synthesis methods affect gold nanoparticle (AuNPs) monodispersity and cytotoxicity. Using single particle inductively coupled plasma mass spectrometry (SP-ICP-MS), we found that the size distribution of AuNPs synthesized with a cetyltrimethylammonium chloride (CTAC) cap was significantly improved compared to AuNPs synthesized with citrate capping agents. We determined an up to 4×decrease in the full width at half maximum (FWHM) value of the normal distributions of AuNP diameter and up to a 12% decrease in relative standard deviation (RSD). While the CTAC-capped AuNPs exhibit narrow nanoparticle size distributions, they are cytotoxic, which limits safe and effective bioanalytical and biomedical applications. We sought to impart biocompatibility to CTAC-capped AuNPs through a PEGylation-based surface ligand exchange. We developed a unique ligand exchange method driven by physical force. We demonstrated the successful PEGylation using various PEG derivatives and used these PEGylated nanoparticles to further bioconjugate nucleic acids and peptides. Using cell viability quantification, we confirmed that the monodisperse PEGylated AuNPs were biocompatible. Our monodisperse and biocompatible nanoparticles may advance safe and effective bioanalytical and biomedical applications of nanomaterials.

Keywords Gold nanoparticles · Single particle ICPMS · Biocompatibility · Bioconjugation · Monodisperse

Introduction

Probing the interactions between nanoparticles and cells remains a primary focus of bioanalytical and nanomedicine research [1–3]. Current investigations have identified that the nanoparticle size and size distributions influence how nanoparticles interact with cells and biological systems [4–6]. The availability of monodisperse and biocompatible nanoparticles is often a prerequisite to enable safe, accurate, and effective applications in research and clinical practice.

Monodisperse nanoparticles are defined by minimal size variation between individual colloidally dispersed nanoparticles. Studies have demonstrated that monodisperse nanoparticles are preferable for improved therapeutic results [7, 8]. In particular, gold nanoparticles (AuNPs) are commonly employed given their relative ease of synthesis and surface modification and their inherent biocompatibility [9]. AuNPs are used in bioanalytical and biomedical contexts as model systems for understanding and probing nanoparticle-cell interactions [10–13]. Additionally, AuNPs have demonstrated a significant ability to serve as carriers for adjuvant delivery or as drivers for photothermal therapy [14]. Further, AuNPs are frequently used for molecular detection and diagnostic assays [15, 16]. Given the continued usage of AuNPs, there is a significant need to understand and improve upon the monodispersity of AuNPs used in research and clinical environments leading up to bioanalytical and biomedical applications.

Alex N. Frickenstein and Shirsha Mukherjee contributed equally to this work.

Published in the topical collection *Young Investigators in (Bio-) Analytical Chemistry 2023* with guest editors Zhi-Yuan Gu, Beatriz Jurado-Sánchez, Thomas H. Linz, Leandro Wang Hantao, Nongnoot Wongkaew, and Peng Wu.

✉ Stefan Wilhelm
stefan.wilhelm@ou.edu

[1] Stephenson School of Biomedical Engineering, University of Oklahoma, Norman, OK 73019, USA

[2] Stephenson Cancer Center, University of Oklahoma Health Sciences Center, Oklahoma City, OK 73104, USA

[3] Institute for Biomedical Engineering, Science, and Technology (IBEST), University of Oklahoma, Norman, OK 73019, USA

Published online: 20 January 2023

To assess nanoparticles' relative size and colloidal stability, batch characterization methods such as light scattering or spectrophotometry can be used [17, 18]. Despite their utility, batch methods do not precisely inform researchers of the differences between nanoparticles on a single-particle basis, making accurate quantification of nanoparticle monodispersity challenging. Two techniques for individual particle measurements stand out, i.e., transmission electron microscopy (TEM) and single particle inductively coupled plasma mass spectrometry (SP-ICP-MS) [19–21]. TEM allows for the exact measuring of individual particle size following appropriate sample preparation and post-imaging analysis. By counting large numbers of nanoparticles, a size distribution is generated that defines nanoparticle monodispersity. SP-ICP-MS techniques are applied in bioanalytical and biomedical studies to characterize nanoparticle mass, size, and concentration or correlating changes in nanoparticles due to solution conditions or biomarker presence [22–25]. SP-ICP-MS performs rapid, continuous measurement of individual nanoparticle mass, generating a mass distribution from collected data. The wider the mass distribution, the more polydisperse the nanoparticle sample is. We have previously demonstrated how SP-ICP-MS may be used to assess changes in nanoparticle aggregation and chemical composition based on changes in mass distribution, indicating the ability of SP-ICP-MS to measure differences in mass distributions effectively [26, 27]. The high-throughput and continuous nature of SP-ICP-MS makes analysis rapid while maintaining high accuracy given its single-particle resolution.

In this study, we demonstrate how AuNPs synthesized between two different methods differ in their monodispersity. From reviewing several reports using AuNPs, we observed an apparent difference in the size distribution between large (> 10 nm) citrate-capped AuNPs and AuNPs capped with cetyltrimethylammonium chloride (CTAC) [28, 29]. If CTAC-capped AuNPs possess a better monodispersity compared to citrate-capped AuNPs, CTAC-capped AuNPs may prove more useful in bioanalytical and biomedical applications [8]. We synthesized citrate-capped and CTAC-capped AuNPs of various diameters and characterized them extensively. Notably, SP-ICP-MS measures were collected to verify any differences in mass, and thus size, distribution between AuNPs. Through this, we demonstrate how SP-ICP-MS techniques can be effectively applied to analyze differences in mass distribution between nanoparticle populations.

It is, however, well known that CTAC is cytotoxic and thus unfit for many applications in bioanalytical and biomedical settings [30, 31]. To overcome this challenge, we implemented a unique physical replacement method that imparts biocompatibility to CTAC-capped AuNPs, increasing their bioanalytical and biomedical relevance. Using SP-ICP-MS quantification, we demonstrated that our physical replacement method did not change the mass distribution of CTAC-capped AuNPs. Finally, we showed how through conjugating the appropriate ligand during our physical replacement method, CTAC-capped AuNPs could be made bio-functional by conjugating thiolated nucleic acids or peptides. Further, we performed cell uptake experiments to find that when surface chemistries are matched, CTAC-capped AuNPs demonstrate similar performance to citrate-capped AuNPs, which are more commonly used in bioanalytical and biomedical contexts.

Our study shows the significant difference between the monodispersity of AuNPs synthesized by different methods. Further, we demonstrate how SP-ICP-MS is a valuable tool for quantifying and comparing the monodispersity between nanoparticle populations. Additionally, we illuminate how physical replacement methods of nanoparticle surface ligands may be applicable for improving the biocompatibility of highly monodisperse CTAC-capped AuNPs. The combination of our findings offers new means by which highly monodisperse AuNPs may be synthesized, characterized, and surface modified for downstream use in bioanalytical and biomedical applications.

Experimental section

Materials

We used aqueous gold(III) chloride trihydrate ($HAuCl_4$, Sigma-Aldrich 520,918), sodium citrate tribasic dihydrate (Sigma-Aldrich S4641), hydroquinone (Sigma-Aldrich, Reagent Plus, ≥ 99.0%), cetyltrimethylammonium bromide (CTAB, Sigma-Aldrich H6269), sodium borohydride ($NaBH_4$, 213462), cetyltrimethylammonium chloride (CTAC, Sigma-Aldrich 292737), and L-ascorbic acid (AA, Sigma-Aldrich 255564) to synthesize gold nanoparticles (AuNPs) using different methods. We cleaned Glassware for synthesis and digested cell samples for ICP-MS using hydrochloric acid (HCl, Sigma-Aldrich ACS reagent 37%) and nitric acid (HNO_3, Sigma-Aldrich ACS reagent 70%). We used Tween 20 (Sigma-Aldrich P9416) during the centrifugation and purification of AuNPs. We PEGylated AuNPs using 5-kDa methoxy-PEG-thiol (mPEG-SH, Laysan Bio) or 5-kDa maleimide-PEG-OPSS (malPEG-OPSS, Laysan Bio). TEM imaging was completed on copper TEM grids with carbon film (Ted Pella, 01813-F).

We used DNA strands from Integrated DNA Technologies (IDT). We composed DNA storage and reaction buffers using mixtures of tris(hydroxymethyl)aminomethane ACS reagent ≥ 99.8% (Tris, Sigma-Aldrich 252859), ethylenediaminetetraacetic acid BioUltra, anhydrous ≥ 99% (EDTA, Sigma-Aldrich EDS), or sodium chloride (NaCl S7653). We purified DNA using illlustra NAP-5 columns (GE Healthcare

17–0853-01). We implemented the peptide K7C (Biomatik, amino acid sequence N'-C' KKKKKKKC) to improve cell uptake of AuNPs in cells.

In preparing RAW 264.7 macrophages for confocal laser scanning microscopy (CLSM), we used NucBlue DAPI (Invitrogen R37606) to label cell nuclei and wheat germ agglutinin CF488A (WGA, Biotium 29024) to label glycoproteins on cell membranes. We suspended both labeling agents in 1 × Hank's balanced salt solution (HBSS, Gibco 14185–052) in 1 × phosphate buffered saline (PBS, Thermo Fisher BP3994). We cleaned the microscopy coverslips using a mixed solution of hydrogen peroxide (H_2O_2, Sigma-Aldrich 216763) and sulfuric acid (H_2SO_4, Avantor 7664–93-9).

Instrumentation

CTAC-capped AuNP synthesis was performed using Harvard Apparatus PHD ULTRA syringe pumps (Harvard Apparatus 703,005). Vortexing steps for physical replacement PEGylation were carried out using VWR® Analog Vortex Mixers (Avantor 10153–838). Dynamic light scattering (DLS) and zeta potential measurements were carried out on a Malvern Zetasizer NanoZS. Ultraviolet–visible spectrophotometry measurements were performed using a UV–Vis-NIR spectrophotometer (Agilent Cary 5000). Transmission electron microscopy (TEM) images were collected on a JEOL 2010F Field Emission TEM with a Direct Electron DE-12 camera. We conducted SP-ICP-MS analysis of AuNPs using a PerkinElmer NexION 2000 ICP-MS instrument with a single cell introduction system (PerkinElmer N8150032) and the PerkinElmer Single Cell Application software. We performed confocal microscopy imaging using a ZEISS LSM 880 inverted CLSM with a photomultiplier tube (PMT) detector, a 405-nm diode laser, a 488-nm argon laser, and a 561-nm diode-pumped solid-state laser for fluorescent channels through a main beam splitter (MBS) 488/561/633 filter.

Synthesis of gold nanoparticles by different methods

All gold nanoparticle synthesis was performed in glassware cleaned by Aqua Regia, comprised of a 3:1 v/v ratio of hydrochloric acid and nitric acid. Fourteen-nanometer citrate-capped AuNP seeds were synthesized according to the Frens/Turkevich method, whereby ionic gold is reduced into solid gold via citrate at high temperatures [32]. These 14-nm seeds were used to grow larger quasi-spherical AuNPs based on methods developed by Perrault and Chan [28]. By varying the molar ratio of $HAuCl_4$ to 14-nm AuNP seeds, the final size of grown AuNPs could be controlled (Table S1). This method targeted the synthesis of AuNPs of diameters 30 nm, 45 nm, and 60 nm. The AuNPs were purified by centrifugation after growth and resuspended in a 0.01% citrate, 0.1% Tween 20 solution before characterization and surface modification.

The CTAC-capped AuNPs were synthesized using previously developed methods [29, 33, 34]. First, gold clusters were synthesized by reducing Au^{3+} ions with $NaBH_4$ in a concentrated cetyltrimethylammonium bromide (CTAB) solution. These clusters were then used to synthesize 10-nm CTAC-capped AuNPs needed to grow larger CTAC-capped AuNPs. The growth process for CTAC-capped AuNPs differs from that of citrate-capped AuNPs as it uses CTAC as the stabilizing agent and ascorbic acid at 35 °C as the reducing agent. Further, the precursor Au^{3+} ions were added dropwise via a syringe pump setup. The size of grown AuNPs was predicted by controlling the moles of seeds used in the growth reaction (see Table S2). The CTAC-capped AuNPs of 15-nm, 30-nm, 45-nm, and 60-nm target diameters were synthesized using these methods. Following growth, CTAC-capped AuNPs were purified by centrifugation and resuspended in 20-mM CTAC solution before characterization and surface modification. For more details on the AuNP synthesis methods, see the ESM.

Nanoparticle characterization

Initial characterization of the synthesized AuNPs was performed using dynamic light scattering (DLS), ultraviolet–visible spectrophotometry (UV–Vis), and transmission electron microscopy (TEM). The DLS techniques measured the hydrodynamic diameter and surface zeta potential of the synthesized AuNP before and after surface modification. These measurements also provided an initial indication of polydispersity through the polydispersity index (PDI) value. Generally, nanoparticles possessing a PDI < 0.1 are colloidally stable and monodisperse; this arbitrary metric was considered when evaluating synthesis success. The UV–Vis measurements were used to determine the extinction spectrum of each nanoparticle dispersion and to estimate the nanoparticle molar concentrations [28]. We further prepared TEM micrographs of the synthesized AuNPs and collected TEM images of each AuNP population. Images were analyzed using ImageJ, and typically > 150 AuNPs were counted and measured to determine the distribution of AuNP diameters for a given synthesized nanoparticle population.

SP-ICP-MS measurements of synthesized gold nanoparticles

Recently, we have demonstrated how SP-ICP-MS is useful for accurately and rapidly measuring nanoparticle mass and size distributions [2, 26, 27]. In the current study, we used

SP-ICP-MS to identify the mass distribution of synthesized AuNPs and corroborate the size distribution data observed from our TEM imaging studies. All measurements were collected using a PerkinElmer NexION 2000 ICP-MS with a high-efficiency sample-introduction system comprised of a nebulizer, spray chamber, and a heating element wrapped around the spray chamber. The heating element limits condensation on the interior of the spray chamber, improving the transport efficiency (TE) of introduced AuNPs. We optimized the instrument settings for SP-ICP-MS measurements (see Table S3). We measured the TE using commercially available Lu175-doped polystyrene beads and found the TE to be ~ 70%. Using a set of AuNP standards of known diameter, we created a particle calibration that correlated Au^{3+} signal intensity to Au mass in attograms (ag), allowing for immediate translation of the intensity of individual Au events into an estimated particle mass. Prior to measurements of prepared samples, we significantly diluted the AuNPs to ~ 3×10^{-16} M in nanopure water to minimize matrix effects between samples and to minimize any potential signal overlap that would result from multiple AuNPs being detected simultaneously [35–37]. Dilute AuNPs were then introduced into the instrument via a microfluidic introduction system, and correlating mass distributions were collected. We then translated the mass distribution of each AuNP into a correlating size distribution to gain further insights into the monodispersity of the measured AuNPs.

PEGylation of gold nanoparticles

Modifying the surface of citrate-capped AuNPs with thiolated or disulfide-modified PEG ligands was performed according to prior methods [38]. Room temperature incubation of AuNPs in a solution of PEG and Tween 20 for 30 min was sufficient to complete PEGylation of the AuNP surface. A PEG density of 7 PEG/nm^2 was targeted for each PEGylation procedure. Note: seven PEG per nanoparticle surface area in nm^2 unit is the amount of PEG molecules added to the citrate-capped AuNPs.

The PEG molecules, however, do not readily bind to the surface of CTAC-capped molecules and therefore require an alternative conjugation method. Our approach was inspired by prior studies using physical methods to displace cetyltrimethylammonium-based positively charged ligands from gold-based nanomaterials [39, 40]. In this "physical replacement" method, CTAC-capped AuNPs are spun down into concentrated pellets via centrifugation. The supernatant is removed, and the pellet is suspended in 50 µL of a concentrated solution of PEG in 0.1% Tween 20. The solution is sonicated for 1 min and then vortexed vigorously for 30 s. The resulting AuNP solutions were then diluted to 1 mL in a 0.1% Tween 20 solution before purification by centrifugation. This process was repeated twice for three iterations of sonication, vortexing, and centrifugation. The concentration of PEG used at each step was such that after the three repetitions of the process, the final added PEG amount would be 7 PEG/nm^2.

We characterized all PEGylated AuNPs by DLS to affirm PEG presence. Further, we collected zeta potential measurements of pre- and post-PEGylation AuNPs to demonstrate successful surface charge changes. We also performed UV–Vis and SP-ICP-MS measurements of AuNPs to ascertain how our "physical replacement" method may induce changes in AuNP extinction spectra or mass distribution. For more details on PEGylation methods, see the ESM.

Biofunctionalization via maleimide-thiol conjugation

Previous studies have demonstrated that conjugating PEG with maleimide functional groups can be used to conjugate thiolated ligands to the surface of nanoparticles [38, 41]. Applying this technique to CTAC-AuNPs would increase the versatility of these monodisperse model nanoparticles beyond PEG functional groups. Thus, as described, we performed PEGylation of 60-nm CTAC-capped AuNPs using 5-kDa maleimide PEG-OPSS (malPEG) and confirmed the PEG presence using DLS measurements. After centrifuging PEGylated AuNPs to remove any excess malPEG, the resulting AuNP pellet was dispersed in a concentrated solution of either thiolated peptide K7C (amino acid sequence of KKKKKKKC) or thiolated single-stranded DNA (ssDNA) molecules (see Table S4). We selected these ligands based on prior studies [38, 42, 43]. For ssDNA and K7C, the concentration of ligands in solution added to malPEG-AuNPs was such that there would be a maximum of 7 ligand molecules per nm^2 on the AuNP surfaces. After allowing the mixture to incubate overnight at room temperature, we took DLS measurements to confirm changes in hydrodynamic diameter associated with the conjugation of K7C or ssDNA.

We performed additional experiments depending on the ligand conjugated to confirm successful conjugation via maleimide-thiol click chemistry further. For K7C, in vitro experiments using various cell lines were performed. For ssDNA, we created DNA-AuNP superstructures by conjugating ssDNA of two different sequences to either 60-nm or 15-nm diameter AuNPs. The conjugated ssDNA is complementary to different sections of a third "linker" ssDNA strand. After washing off excess ssDNA, one DNA-AuNP population would be hybridized to the linker through previously defined methods [42]. We centrifuged the resulting linker-DNA-AuNP complex multiple times to remove excess linker ssDNA strands. Then, we introduced the other DNA-AuNP population, which binds to the other available section of the linker, forming a "core-satellite" AuNP-DNA-AuNP

superstructure. The resulting superstructures were characterized by DLS and TEM. For more details on maleimide-thiol conjugation steps, see the ESM.

Cell viability of PEGylated gold nanoparticles

To verify the complete removal of cytotoxic CTAC from the CTAC-capped AuNPs via our unique physical replacement approach, we performed commercially available XTT viability assays for DC2.4 murine dendritic cells and RAW 264.7 murine macrophages. Ninety-six-well plates with either 10,000 DC2.4 cells/well or 22,000 RAW 264.7 cells/well were prepared in appropriate media and treated with 0.1 nM of 60-nm AuNPs in media and incubated for 24 h. The AuNP groups included citrate-capped AuNPs, CTAC-capped AuNPs, and citrate- and CTAC-capped AuNPs that underwent their respective PEGylation methods. Media-only and cell-only wells were included for negative controls. Following treatment incubation, an XTT cell viability assay was performed on all wells, and absorbance was measured to assess relative cell viability according to the manufacturer's instructions. For more details on cell culturing and XTT viability assay methods used, see the ESM.

Cell uptake of biofunctionalized gold nanoparticles

The K7C peptide is a model positively charged biomolecule that has been reported to increase AuNP uptake in cells [2, 38]. We sought to demonstrate that CTAC-capped AuNPs modified with malPEG and conjugated to K7C would demonstrate similar uptake results compared to citrate-capped AuNPs of the same surface chemistry. We first affirmed our malPEG-K7C AuNP conjugates maintained biocompatibility via an XTT viability assay using RAW 264.7 murine macrophages. PEGylated or malPEG-K7C AuNPs synthesized by citrate-capped or CTAC-capped methods (4 total groups) treatments in media (0.1 nM) were added to 22,000 cells/well and incubated for 3 h. The CTAC molecules were used as positive controls for this experiment, and results were compared to media-only and cell-only negative controls. Following incubation, wells were treated with XTT viability agents, and absorbance was measured.

Based on the XTT viability results, we sought to assess the uptake of our AuNPs by RAW 264.7 murine macrophages using confocal laser scanning microscopy (CSLM) and ICP-MS. For CLSM, 0.01 nM of AuNPs in media were used to treat 15,000 cells/well in 24-well plates with coverslips. This lower AuNP concentration was selected as it would not impact cell viability and would limit the saturation of the scattering signal from CSLM. After 3 h of incubation, coverslips were stained to fluorescently tag cell membranes and nuclei according to previously defined methods [2]. Coverslips were then imaged using a ZEISS LSM 880 inverted CLSM. The AuNPs were detected by light scattering from the laser [2, 10].

Cell uptake of AuNPs was measured using previously defined ICP-MS methods [10]. Briefly, RAW 264.7 cells were seeded in a 48-well plate with 200,000 cells/well and treated with 0.01 nM AuNPs in media. The lower AuNP concentration was selected to limit the possibility of saturating the ICP-MS detector. After 3 h, wells were rapidly washed once with a dilute gold etchant (KI/I_2) solution to remove any AuNPs not internalized by cells [2, 10]. Then, wells were washed with 1xPBS, and the well contents were digested in 500 µL aqua regia (4:1 v/v HNO_3:HCl). The digested solution (125 µL) was diluted in nanopure water and measured using standard ICP-MS to measure the Au content of each sample. The Au intensity signal was compared against the Mg intensity signal used to estimate the cell number, and calibration curves for both ions were used to calculate the number of AuNPs and the number of cells in each sample. To account for any AuNPs stuck to well plates, the same process was performed on a plate with no cells using the same AuNP treatments, incubation time, and wash steps. The ICP-MS signal from these wells was subtracted from the signal from the cell data, so only cell-associated AuNPs were counted. For more details on methods used for CSLM and ICP-MS preparation and data collection, see the ESM.

Results and discussion

Mass and size distributions of gold nanoparticles

We synthesized AuNPs by the citrate-capping and CTAC-capping methods and initially characterized AuNPs by DLS, UV–Vis, and TEM (Fig. 1). To synthesize CTAC-capped AuNPs, we followed the multi-step process reported in prior studies and characterized both the Au-clusters (Fig. S1) and the 10-nm CTAC-capped AuNP seeds (Fig. S2) [29, 34]. For DLS data of synthesized AuNPs, it is important to consider that the diameter reported is the hydrodynamic diameter, which includes surface ligands and behavior that influence particle Brownian motion [44]. Thus, hydrodynamic diameter estimates are typically larger than the desired or expected AuNP diameter. With this consideration, we observed that the hydrodynamic diameter estimates align with our targeted AuNP diameter during synthesis (Fig. 1a–b).

The UV–Vis characterization can further indicate AuNP size and stability based on the nanoparticles' surface plasmon resonance. Additionally, UV–Vis extinction spectral analysis is useful for estimating AuNP concentration. The Beer-Lambert Law is a valuable method for estimating AuNP molar

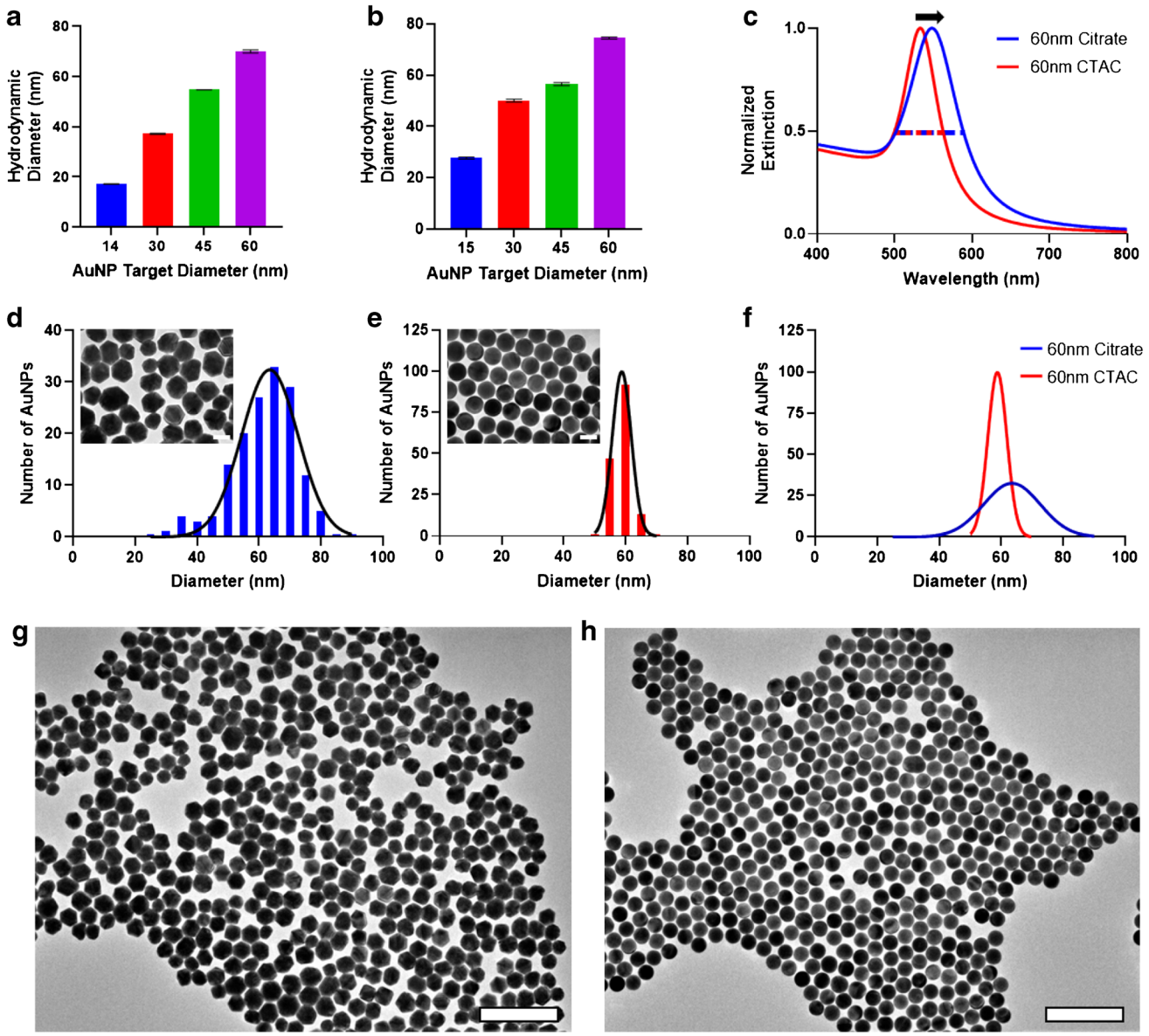

Fig. 1 Physicochemical characterization of synthesized AuNPs. **a** DLS measurements of synthesized citrate-capped AuNPs. **b** DLS measurements of synthesized CTAC-capped AuNPs. Colored bars for **a** and **b** represent the measured mean hydrodynamic diameter for synthesized AuNPs of different target diameters. Error bars for **a** and **b** show standard deviation from N = 3 measurements. **c** The UV–Vis extinction spectrum for 60-nm diameter citrate-capped AuNPs differs from that of the UV–Vis extinction spectrum for CTAC-capped AuNPs of the same diameter. **d–e** TEM micrograph images and size distributions of 60-nm diameter citrate-capped and CTAC-capped AuNPs. Colored bars indicate the number of AuNPs (i.e., frequency) of each diameter listed on the x-axis. Black lines indicate the Gaussian normal distribution. Size distributions were normalized to $N = 150$ AuNPs for each distribution. The scale bar is 50 nm. **f** Overlay of the Gaussian normal distributions for 60-nm AuNPs by both capping methods demonstrating the difference in particle size distribution height and width. **g–h** Low magnification TEM micrographs of 60-nm diameter citrate- and CTAC-capped AuNPs, respectively. The scale bar is 300 nm

concentrations based on measured UV–Vis extinction spectra of the AuNP colloidal dispersions [28]. This remains the case for CTAC-synthesized AuNPs. Despite the difference in UV–Vis spectra between citrate- and CTAC-synthesized AuNPs (Fig. S3), we applied the Beer-Lambert Law for calculating the nanoparticle concentration given that a primary driver of differences in the AuNP molar extinction coefficient is size [28]. Interestingly, the peak extinction wavelength and spectral width of all synthesized CTAC-capped AuNPs differed from citrate-capped AuNPs of the same size in that CTAC-capped AuNPs possessed a lower peak extinction wavelength and a narrower spectral width (Fig. 1c, Table 1). We attribute this phenomenon to how nanoparticle size and size distributions contribute to extinction [45, 46]. For

citrate-capped AuNPs, a greater proportion of AuNPs is larger than the target diameter, as shown by the TEM size distributions (Fig. 1d–e, Fig. S4). The larger particles in the citrate-capped AuNP population may contribute substantially to the overall extinction spectrum, resulting in a red shift of the peak extinction wavelength and the spectrum width. By comparison, CTAC-capped AuNPs possess AuNPs that are primarily of the target diameter, minimizing "off-target" extinction. Our observations of the difference in extinction spectra indicate the AuNPs initially synthesized to be CTAC-capped may prove useful in bioanalytical and biomedical applications that could rely on small changes in extinction spectra to identify molecule presence [16] or solution conditions [27].

We collected TEM micrographs of each particle population to quantify AuNP size distributions (Fig. 1d–f, Fig. S4). Before measuring size distributions, we observed a striking difference in AuNP shape and monodispersity by TEM (Fig. 1g–h). We attribute this difference primarily to how Au^{3+} ions are reduced onto the surface of the precursor AuNP seeds and the differing surface chemistries of the precursor AuNP seeds. For CTAC-capped AuNPs, Au^{3+} ions are added dropwise to the reaction solution, permitting gradual AuNP growth. Further, the bilayer nature of the amphiphilic CTAC molecules on the surface of the AuNPs as they grow serves to maintain a spherical AuNP shape. By comparison, the rapid nature by which Au^{3+} is added for citrate-capped AuNPs as well as the less constraining nature of citrate on the surface of precursor AuNPs results in quasi-spherical AuNPs of a wider shape and size variety.

In addition to calculating the approximate mean diameter values for each particle population using ImageJ, we applied a normal Gaussian distribution to the diameter distribution to assess the relative polydispersity. We quantified polydispersity through measuring the full width at half maximum (FWHM) of each distribution according to Eq. 1:

$$FWHM \approx 2.355 * \sigma \tag{1}$$

where σ is the standard deviation of the Gaussian normal distribution.

This quantification of nanoparticle polydispersity is used in the literature and provides insight into the relative size differences between nanoparticles in solution [8]. For each target size except the 14-nm citrate-capped and 15-nm CTAC-capped AuNPs, there is an evident difference in the FWHM values (Table 1). Namely, the FWHM values for CTAC-capped AuNPs are lower than that of citrate-capped AuNPs by up to four times. Interestingly, we observed that the difference in FWHM values becomes more apparent with increasing AuNP diameter. The larger the target AuNP diameter, the more monodisperse the CTAC-capped AuNPs are compared to the citrate-capped AuNPs. We demonstrate this phenomenon clearly in Fig. 1f.

As another metric for nanoparticle monodispersity, we calculated the relative standard deviation (RSD) using Eq. 2:

$$RSD = \frac{100 * \sigma}{\mu} \tag{2}$$

where RSD is reported as a perfect (%) value and μ is the mean diameter of the normal distribution for the nanoparticle population. The RSD values are often used to assess nanoparticle monodispersity, with lower RSD values indicating a greater degree of monodispersity [8, 47]. For each comparison between citrate-capped and CTAC-capped AuNPs, we found that the RSD value was lower for the CTAC-capped AuNPs than for the citrate-capped AuNPs. The magnitude of the difference was as high as ~ 12%, with the difference increasing directly with AuNP diameter. These RSD trends align with those observed from the FWHM observations, further corroborating the improved monodispersity of CTAC-capped AuNPs compared to citrate-capped AuNPs.

Imaging with TEM is limited in its ability to characterize numerous nanoparticles in a high-throughput manner. To overcome this limitation, we performed quantitative SP-ICP-MS analysis to provide additional insight into the mass and size distributions for synthesized AuNPs.

Table 1 Physicochemical characterization results for synthesized AuNPs

Target AuNP diameter (nm)	Synthesis method	Hydrodynamic diameter[#] (nm)	Polydispersity index[#] (PDI)	Peak extinction wavelength (nm)	TEM AuNP Diameter[#] (nm)	TEM FWHM (nm)	TEM RSD (%)
14	Citrate	17.2 ± 0.1	0.02 ± 0.02	518	13.1 ± 1.2	2.8	9.0
30	Citrate	37.2 ± 0.2	0.05 ± 0.02	525	29.2 ± 5.3	12.5	18.1
45	Citrate	54.8 ± 0.0	0.08 + 0.01	533	46.3 ± 6.5	15.3	14.1
60	Citrate	70.0 ± 1.0	0.08 + 0.01	548	62.1 ± 9.7	22.7	15.5
15	CTAC	27.7 ± 0.4	0.09 ± 0.01	527	15.3 ± 1.1	2.7	7.4
30	CTAC	50.1 ± 0.6	0.05 + 0.02	526	35.5 ± 3.3	7.7	9.2
45	CTAC	56.5 ± 0.6	0.02 + 0.01	526	42.2 ± 1.5	3.6	3.7
60	CTAC	74.5 ± 0.4	0.04 + 0.02	533	59.3 ± 2.4	5.6	4.0

[#]Mean value ± standard deviation

We used an AuNP calibration curve made by measuring synthesized AuNP standards to correlate individual event ion signals with AuNP mass distributions (Fig. S5). With this calibration curve, accurate mass distributions for all AuNPs were generated (Fig. 2a–c, Fig. S6). The SP-ICP-MS technique measures the mass of individual particles, which we converted into an estimated AuNP diameter by assuming a spherical AuNP (Eq. 3).

$$D = \sqrt[3]{\frac{6 * m}{\pi * \rho}} \tag{3}$$

In Eq. 3, D is the calculated AuNP diameter, m is the particle mass as measured by SP-ICP-MS, and ρ is the density of the particle composite material ($\rho = 19.3 \frac{g}{cm^3}$ for Au).

From the mass distributions measured by SP-ICP-MS and using Eq. 3, we estimated the apparent size distributions for each AuNP population (Fig. 2d–e, Fig. S7).

The results from SP-ICP-MS corroborate those found in TEM, i.e., CTAC-capped AuNPs possess tighter mass distributions compared to citrate-capped AuNPs. Further, we observed that the general FWHM and RSD trends from the TEM analysis are similar to those seen in the SP-ICP-MS mass and size distributions (Table 2). CTAC-capped AuNPs generally possess lower FWHM and RSD values. We noted an exception to the previous TEM data in the case of the citrate-capped 14-nm AuNPs and the CTAC-capped 15-nm AuNPs, where the mean diameter along with the FWHM and RSD values and trends are all different from those found by TEM. We attribute these results to the fact that these particles are small enough to push the limit of detection of SP-ICP-MS instrumentation and methods [37, 48].

Thus, from both TEM and SP-ICP-MS characterization of the nanoparticles, we see that AuNPs synthesized using the CTAC-capping method possess a greater degree of monodispersity (i.e., narrower mass/size distribution) in comparison to AuNPs synthesized using the citrate-capping method.

Surface modification of gold nanoparticles

While our comparisons of monodispersity promote the use of CTAC-capped AuNPs for bioanalytical and biomedical applications, additional steps must be taken to remove the cytotoxic effects CTAC imposes on these AuNPs. PEGylation is a commonly applied method to improve nanoparticle stability and biocompatibility in biological environments [49, 50]. We performed PEGylation of AuNPs as previously described. We incubated citrate-capped AuNPs with PEG at room temperature, while we PEGylated the CTAC-capped

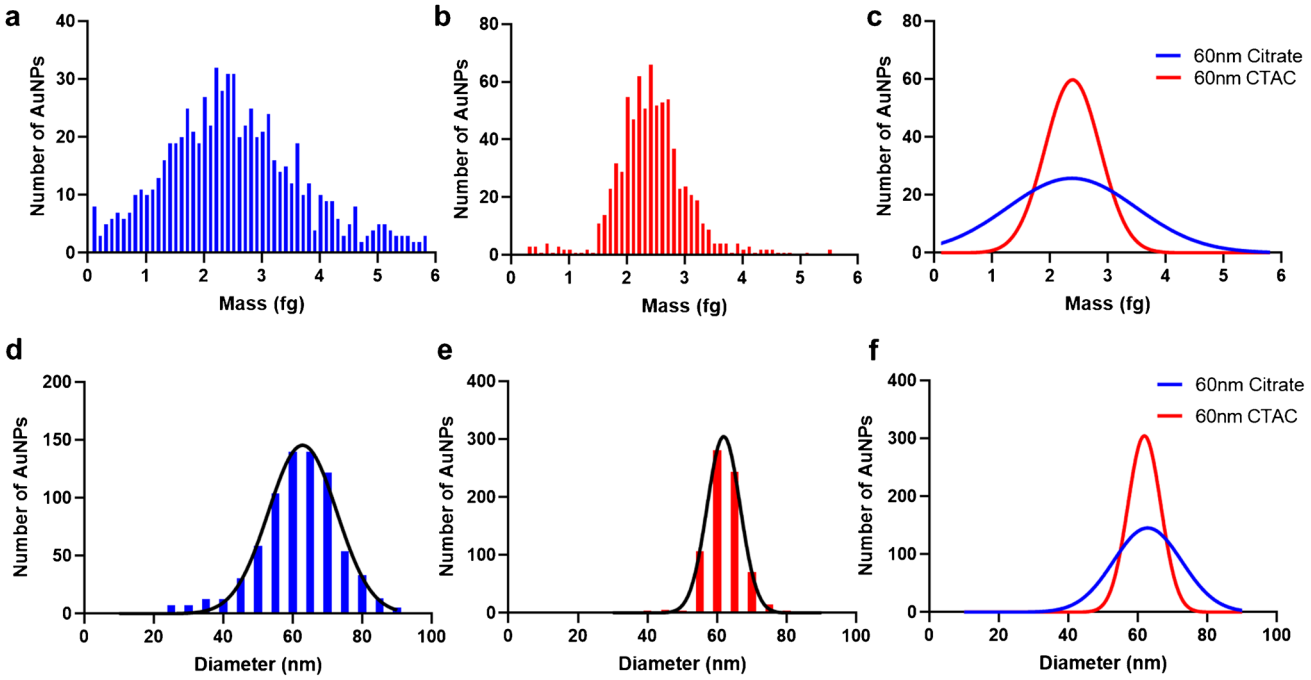

Fig. 2 SP-ICP-MS characterization of synthesized 60-nm diameter AuNPs. **a**–**b** Mass distributions of 60-nm diameter citrate-capped and CTAC-capped AuNPs. Colored bars indicate the number of AuNPs at each mass on the x-axis. Distributions were normalized to $N = 750$ AuNPs. **c** Overlay of Gaussian normal mass distributions of synthesized 60-nm diameter AuNPs demonstrating differences in distribution height and width. **d**–**e** Measured mass distributions were converted into diameter distributions using Eq. 3. Colored bars indicate the number of AuNPs of each diameter n the *x*-axis. Black lines indicate the Gaussian normal distribution. **f** Overlay of Gaussian normal diameter distributions of synthesized 60-nm diameter AuNPs demonstrating differences in distribution height and width

Table 2 SP-ICP-MS characterization results for synthesized AuNPs

Target AuNP diameter (nm)	Synthesis method	Mean mass[#] (ag)	Mass FWHM (ag)	Mass RSD (%)	Mean calculated diameter[#] (nm)	Diameter FWHM (nm)	Diameter RSD (%)
14	Citrate	39 ± 2	4.2	4.6	16.7 ± 0.8	1.9	4.8
30	Citrate	251 ± 169	397.5	67.2	30.1 ± 6.0	14.2	20.1
45	Citrate	923 ± 527	1241.1	57.1	45.9 ± 8.9	21.0	19.4
60	Citrate	2379 ± 1114	2623.5	46.8	62.8 ± 9.8	23.1	15.6
15	CTAC	67 ± 18	42.6	27.1	18.8 ± 1.8	4.2	9.6
30	CTAC	379 ± 133	312.3	35.0	34.5 ± 4.7	11.1	13.6
45	CTAC	681 ± 144	339.1	21.1	40.6 ± 3.2	7.5	7.9
60	CTAC	2391 ± 476	1121.0	19.9	61.9 ± 4.7	11.1	7.6

[#]Mean value ± standard deviation

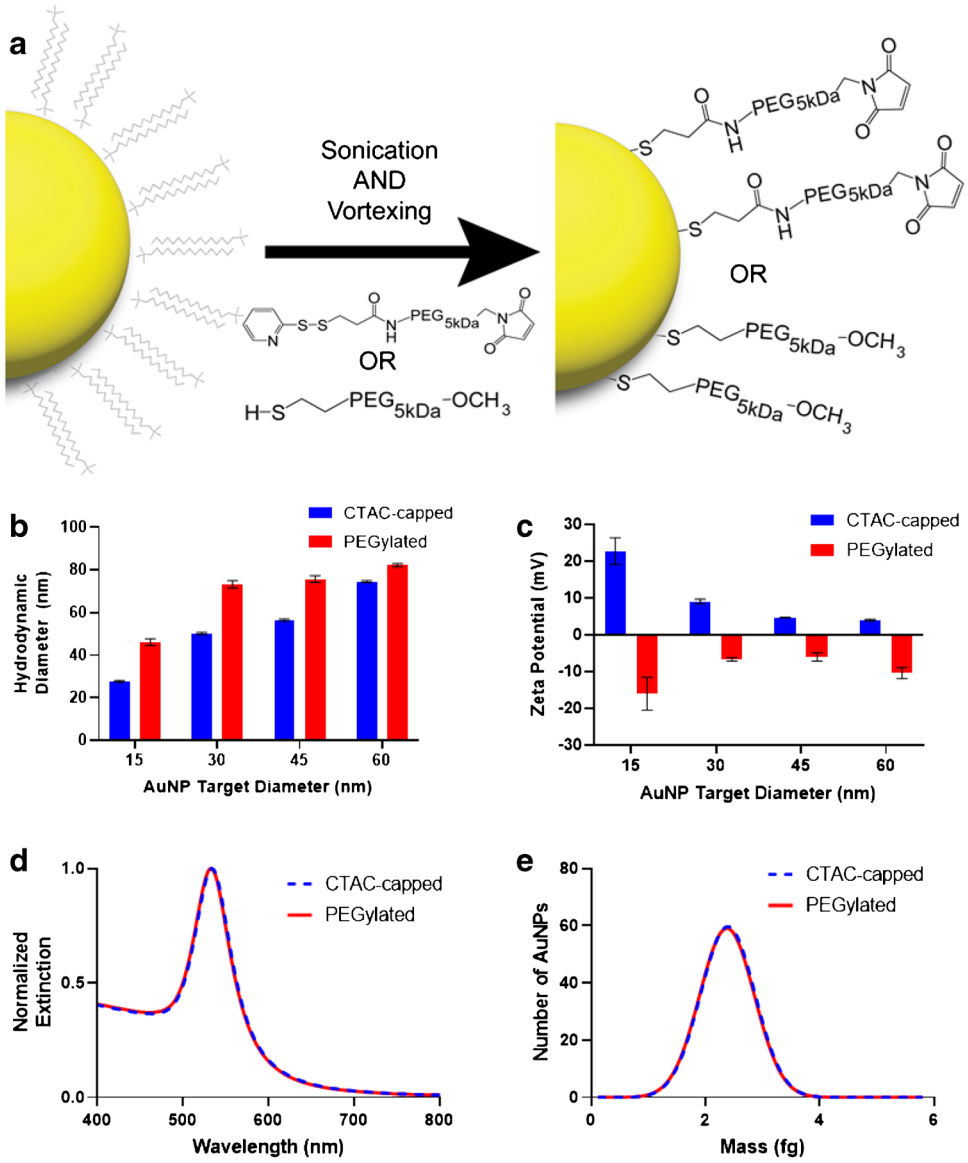

Fig. 3 PEGylation of CTAC-capped AuNPs is possible by applying physical force. **a** Schematic demonstrating the transition from CTAC-capped to PEG-conjugated AuNP surface chemistry using either 5-kDa mPEG-SH or 5-kDa malPEG-OPSS. **b** DLS data demonstrating an increase in hydrodynamic diameter following PEGylation of CTAC-capped AuNPs with 5-kDa mPEG-SH. Error bars indicate the standard deviation for three measurements. **c** Zeta potential measurements of CTAC-capped AuNP before and after PEGylation. Error bars indicate the standard deviation for three measurements. **d** UV–Vis extinction spectra of 60-nm diameter CTAC-capped AuNPs before and after PEGylation, demonstrating no change in extinction from PEGylation. **e** SP-ICP-MS Gaussian normal distribution of 60-nm diameter CTAC-capped AuNPs before and after PEGylation, demonstrating no change in the mass distribution from PEGylation. Mass distributions were normalized to $N = 750$ AuNPs

Table 3 DLS results of nanoparticles with PEG and PEG-biomolecule conjugation

Nanoparticle sample	Hydrodynamic diameter[#] (nm)	Polydispersity index[#] (PDI)
15-nm CTAC mPEG	46.2 ± 1.5	0.06 ± 0.04
15-nm CTAC malPEG-DNA	51.8 ± 4.7	0.10 ± 0.04
30-nm CTAC mPEG	73.2 ± 1.7	0.02 ± 0.01
30-nm CTAC malPEG-DNA	77.2 ± 1.8	0.05 ± 0.01
45-nm CTAC mPEG	75.7 ± 1.6	0.02 ± 0.01
45-nm CTAC malPEG-DNA	78.1 ± 1.1	0.04 ± 0.04
60-nm CTAC mPEG	82.2 ± 0.8	0.03 ± 0.02
60-nm CTAC malPEG-DNA	94.9 ± 1.6	0.03 ± 0.02
60-nm CTAC malPEG-DNA-linker	99.9 ± 1.8	0.03 ± 0.02
60-nm CTAC Superstructure	152.0 ± 6.4	0.09 ± 0.05
60-nm CTAC malPEG-K7C	90.6 ± 0.6	0.05 ± 0.03

[#]Mean value ± standard deviation

AuNPs using our unique physical replacement approach. The CTAC interactions with AuNPs occur via electrostatic interactions between the positively charged CTAC molecules and the AuNP surface. In our physical replacement approach, CTAC is replaced by PEG molecules that covalently bind to the gold surface through Au–S interactions [51, 52]. With repeated washing of AuNPs and introduction of PEG in multiple steps, all CTAC is effectively removed and replaced with biocompatible PEG molecules covalently bound to the AuNP surface (Fig. 3a).

We confirmed the successful conjugation of mPEG-SH based on our DLS measurements, indicating an increase in hydrodynamic diameter (Fig. 3b and Table 3). We attempted to confirm the PEG layer presence through TEM imaging of negatively stained AuNPs, but there was no apparent difference between CTAC-capped AuNPs before or after PEGylation (Fig. S8). However, zeta-potential quantification further confirmed the presence of PEG on the AuNP surface (Fig. 3d). It is known that CTAC-capped AuNPs possess a positive surface charge due to the CTAC on the surface of the AuNPs [40]. Following PEGylation by our physical replacement method, we observed that zeta potential measurements indicated a shift towards neutral charge values associated with mPEG-SH. Remarkably, our physical displacement PEGylation process did not result in a significant change in the UV–Vis extinction spectrum (Fig. 3e) or mass distribution of AuNPs as measured by SP-ICP-MS (Fig. 3f), thus demonstrating that our technique does not change the monodispersity of AuNPs.

Having demonstrated our physical replacement PEGylation method was successful, we sought to expand the possible surface chemistries available to CTAC-capped AuNPs. Previously, we have shown how maleimide PEG-OPSS (malPEG-OPSS) can be used to conjugate thiolated peptides onto the surface of AuNPs [38]. We applied our physical replacement method using malPEG-OPSS and incubated the PEGylated AuNPs overnight with thiolated molecules. Specifically, we performed this first with thiolated single-stranded DNA. We deemed conjugation successful based on increased hydrodynamic diameter as measured by DLS (Fig. 4a, Table 3). We selected single-stranded DNA (ssDNA) strands for our investigation on the basis that they could form DNA-AuNP superstructures as seen in other studies (Table S3) [42, 43]. Using established protocols, we created similar DNA-AuNP superstructures using 60-nm diameter AuNPs and 15-nm diameter AuNPs, as evidenced by both DLS and TEM data (Fig. 4b–c). These results demonstrated how CTAC-capped AuNPs could be made bio-functional with nucleic acids by using PEGylation with malPEG-OPSS and then conjugating thiolated DNA strands to the surface.

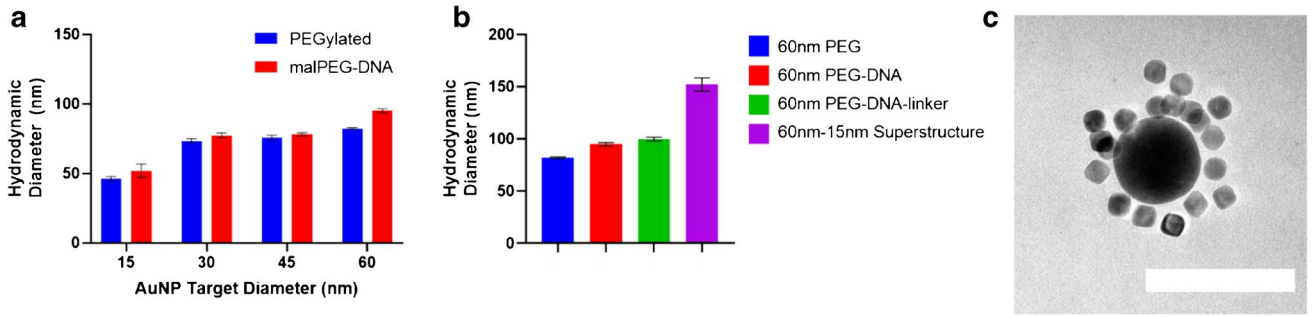

Fig. 4 DNA conjugation to malPEG on the surface of CTAC-synthesized AuNPs. **a** DLS data of CTAC-capped AuNPs following PEGylation with 5-kDa malPEG-OPSS PEG and overnight incubation with thiolated DNA oligos. AuNPs of 15–45-nm diameters were conjugated to DNA strands having the OligoB sequence, while 60-nm diameter AuNPs were conjugated to DNA strands having the OligoA sequence. **b** DLS data of 60-nm CTAC-capped AuNPs after PEGylation with 5-kDa malPEG-OPSS PEG, overnight conjugation with OligoA, hybridization with the "linker" strand, and conjugation to 15-nm AuNP conjugated to malPEG-OligoB. For **a** and **b**, colored bars represent mean hydrodynamic diameter values from $N = 3$ measurements. Black error bars represent the standard deviation from three measurements. **c** TEM micrograph of resulting final DNA-AuNP superstructure. The scale bar is 100 nm

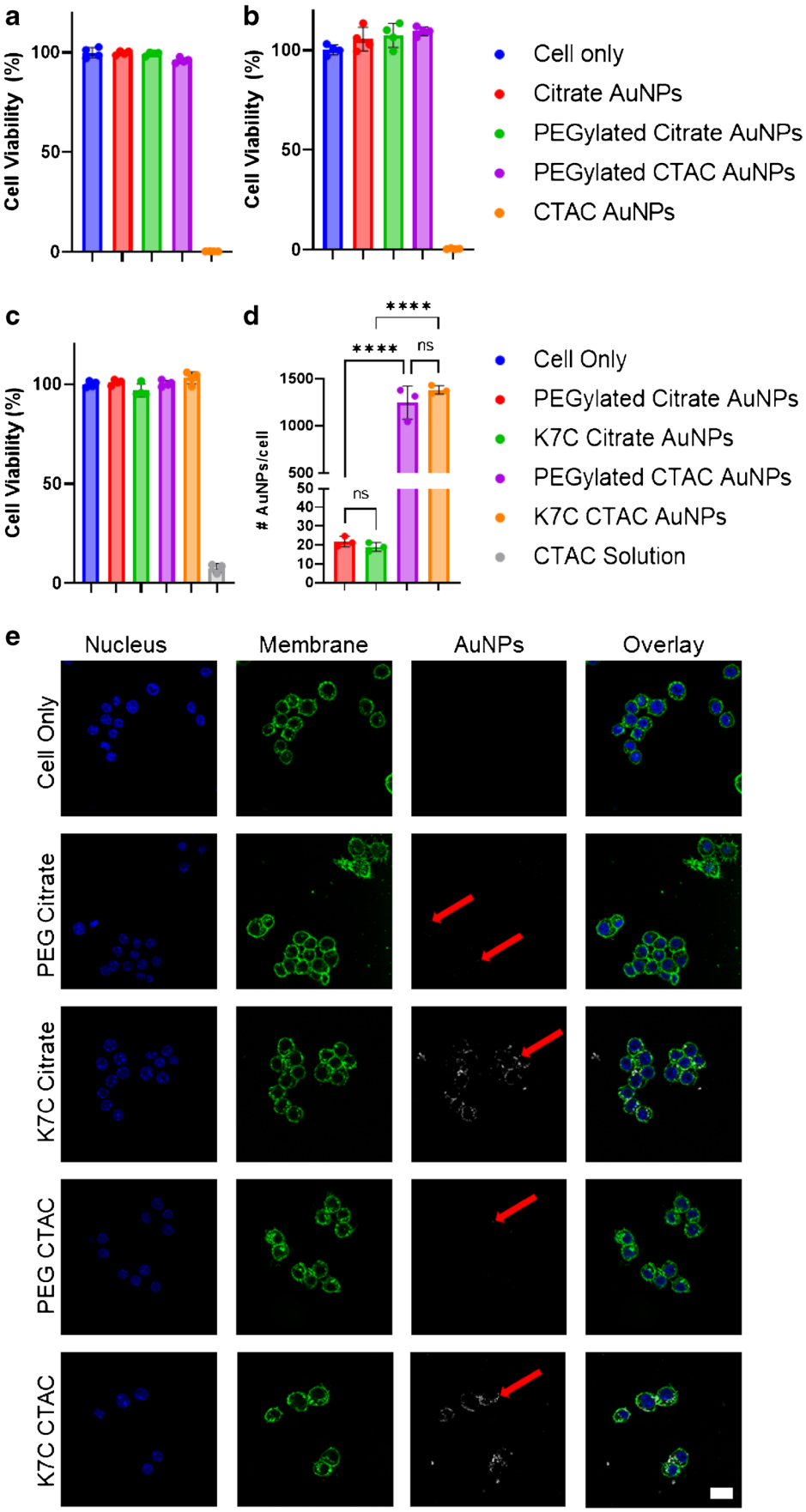

Fig. 5 Cell viability and cell uptake experiments with modified CTAC-capped AuNPs compared to modified citrate-capped controls. **a** XTT cell viability data were collected from DC2.4 cells treated with PEGylated and non-PEGylated AuNPs and incubated overnight. **b** XTT cell viability data were collected from RAW 264.7 cells treated with PEGylated and non-PEGylated AuNPs and incubated overnight. For **a** and **b**, colored bars indicate mean cell viability values for $N=4$ measures for each treatment group. **c** XTT cell viability data were collected from RAW 264.7 cells following 3 h of incubation with AuNPs modified with PEG or with malPEG-K7C conjugates. A CTAC solution was used as a positive control. Colored bars indicate mean cell viability values for $N=3$ measures for each treatment group. **d** ICP-MS estimations of the number of AuNPs/cell for RAW 264.7 cells following the same treatments used in **d**. Colored bars represent mean AuNP/cell values for $N=3$ measurements per treatment group. One-way ANOVA was used to assess the statistical significance between PEG-only AuNPs and K7C AuNPs. ns = no statistical significance, **** = $p<0.0001$. **e** CLSM images of RAW 264.7 cells treated with AuNPs following the same conditions as in **d**. Red arrows point to the scattering signal associated with internalized AuNPs. The scale bar is 20 µm

Biocompatibility and cell uptake of AuNPs

Next, we investigated if our method imparts biocompatibility to the originally CTAC-capped and thus cytotoxic AuNPs. We ran XTT-based cell viability assays with DC2.4 murine dendritic cells (Fig. 5a) and RAW 264.7 murine macrophages (Fig. 5b) following incubation with 60-nm AuNPs for 24 h. Our CTAC-synthesized AuNPs PEGylated with mPEG-SH demonstrated a significantly higher degree of cell viability than as-synthesized CTAC-capped AuNPs in both cell lines. Thus, we confirmed that our method is not only successful in conjugating PEG to the surface of originally CTAC-capped AuNPs, but also that our process removes any cytotoxic CTAC from the surface of the AuNPs.

While the conjugation of PEG to the surface demonstrated improved biocompatibility, the conjugation of additional ligands is essential to improving and understanding interactions between nanoparticles and cells. This bio-functionalization is key to optimizing nanoparticle-cell mechanisms that will enhance bioanalytical and nanomedicine outcomes. As we had previously shown that thiolated biomolecules could bind to malPEG on the surface of AuNPs, we conjugated malPEG to 60-nm AuNP surfaces and then incubated the mixture overnight with the model peptide K7C. In an earlier study, we demonstrated that K7C peptides increase AuNP uptake by cells [2, 38]. We decided to focus our cell uptake and cell viability studies on using 60-nm diameter AuNPs based on nanoparticles of this diameter being favored for cellular uptake, as demonstrated in earlier studies [53]. We first confirmed that a 3-h incubation of RAW 264.7 cells with these K7C-conjugated AuNPs would not affect cell viability (Fig. 5c). Having seen that viability was not affected, we assessed AuNP uptake. We used K7C-AuNPs to treat RAW 264.7 cells that we then imaged using confocal scanning laser microscopy (CLSM) (Fig. 5e). We have previously shown that AuNP uptake by cells can be visualized by CLSM based on the scattering caused by AuNPs [2, 11]. We observed that our CLSM images possess a clear scattering signal associated with AuNPs internalized by the cells, indicating that CTAC-capped AuNPs modified to have K7C surface chemistry demonstrate similar uptake compared to the more commonly applied citrate-capped AuNPs [54, 55].

We then quantified this uptake using ICP-MS methods. In preparing our samples, we noted that CLSM detected an AuNP signal that was not associated with cells. We attribute this signal to AuNPs that stuck to the surface of the coverslip due to the strong positive charge on the AuNP surface from K7C. To remove this background signal for our ICPMS analysis, we washed cells with a dilute gold etchant (KI/I_2) solution. Further, we prepared separate wells without cells that received the same treatment and washing steps. We quantified the gold content of these wells with the gold content of the treated wells that contained cells. We used the measurements from the wells with no cells as the background signal that was subtracted from the signal measured from the wells with cells. Our ICP-MS results demonstrated that RAW 264.7 cells interacted with originally CTAC-capped AuNPs at identical rates ($p > 0.05$) to originally citrate-capped cells for both mPEG-SH and K7C surface chemistries (Fig. 5d). With this, we show that CTAC-capped AuNPs can be applied in bioanalytical and biomedical settings and resolve similar effects to citrate-capped AuNPs.

It is worth considering that the relative number of AuNPs inside cells is dependent on calculations that assume uniform AuNP diameter. ICP-MS measures the mass of Au in each sample, which is then translated into the number of AuNPs using calibration curves and assuming that each individual AuNP possesses the same shape and size (Fig. S9). Thus, the calculations for 60-nm AuNPs tend to be more accurate for CTAC-capped AuNPs than for citrate-capped AuNPs, as demonstrated by the differences in the size distributions we measured in this study. When considering if exact quantification of the number of AuNPs/cell is needed, researchers may look into using CTAC-capped AuNPs for more accurate measures.

Conclusions

In this study, we demonstrated a significant difference between the size distribution (i.e., monodispersity) of AuNPs synthesized by two different methods: citrate-capped and CTAC-capped synthesis. The AuNPs synthesized by the CTAC-capped method demonstrated a significantly narrower size distribution than AuNPs synthesized by the citrate-capped method, indicating a higher degree of monodispersity. While CTAC-capped AuNPs are innately cytotoxic and thus incompatible with many bioanalytical and biomedically relevant systems, we provide a method by which CTAC can be physically replaced with biocompatible PEG molecules without changing the monodispersity of the AuNPs. The PEG molecules used in this process impart biofunctionalization to the AuNPs the PEG is conjugated to, as we showed using maleimide-PEG that conjugates to thiolated peptides or nucleic acids. Compared to the often-used citrate-capped AuNPs, we showed that CTAC-capped AuNPs demonstrate the same uptake behavior in cells when modified to possess the same surface chemistry. Our work additionally demonstrates the value of SP-ICP-MS in assessing monodispersity between AuNPs synthesized using various methods. Further, we demonstrated a possible method by which cytotoxic CTAC ligands may be removed from the surface of monodisperse CTAC-capped AuNPs, increasing their viability for bioanalytical and biomedical research. Continued studies into the utility of SP-ICP-MS for nanoparticle population comparisons are encouraged. We propose that researchers consider using appropriately modified

CTAC-capped AuNPs for bioanalytical and biomedical studies, given their high degree of monodispersity. In particular, we encourage further investigations into alternative surface chemistry modification and ligand functionalization options for CTAC-capped AuNPs.

Supplementary Information The online version contains supplementary material available at https://doi.org/10.1007/s00216-023-04540-x.

Acknowledgements The authors acknowledge the assistance of Dr. Steven Foster, Dr. Preston Larson, Dr. Julian Sabisch, and Dr. Ben Fowler. Additionally, the authors acknowledge the University of Oklahoma (OU) Samuel Roberts Noble Microscopy Laboratory (SRNML), the OU Mass Spectrometry, Proteomics & Metabolomics (MSPM) Core, and the Oklahoma Medical Research Foundation (OMRF) Imaging Core Facility for assistance. The authors would like to thank Sarah Butterfield, Majood Haddad, Luke Whitehead, Nathan Mjema, Abigail Thomas, and Sam Ferguson for their help synthesizing nanoparticles.

Funding This work was supported in part by awards from NIH COBRE (P20GM135009), NSF CAREER (2048130), and OCAST (HR20-106) and by the University of Oklahoma Vice President for Research and Partnerships SRNML Voucher Program.

Declarations

Conflict of interest The authors declare no competing interests.

References

1. Donahue ND, Acar H, Wilhelm S. Concepts of nanoparticle cellular uptake, intracellular trafficking, and kinetics in nanomedicine. Adv Drug Delivery Rev. 2019;143:68–96. https://doi.org/10.1016/j.addr.2019.04.008.
2. Donahue ND, Sheth V, Frickenstein AN, Holden A, Kanapilly S, Stephan C, et al. Absolute quantification of nanoparticle interactions with individual human b cells by single cell mass spectrometry. Nano Lett. 2022;22(10):4192–9. https://doi.org/10.1021/acs.nanolett.2c01037.
3. Villanueva-Flores F, Castro-Lugo A Fau - Ramírez OT, Ramírez Ot Fau - Palomares LA, Palomares LA. Understanding cellular interactions with nanomaterials: towards a rational design of medical nanodevices. Nanotechnology. 2020;31(1361–6528). https://doi.org/10.1088/1361-6528/ab5bc8.
4. Hoshyar N, Gray S, Han H, Bao G. The effect of nanoparticle size on in vivo pharmacokinetics and cellular interaction. Nanomedicine. 2016;11 (6)(1748–6963). https://doi.org/10.2217/nnm.16.5.
5. Thomas OS, Weber W. Overcoming physiological barriers to nanoparticle delivery—are we there yet? Front Bioeng Biotechnol. 2019;7:415. https://doi.org/10.3389/fbioe.2019.00415.
6. Chen K-H, Lundy D, Toh E-W, Chen C-H, Shih C, Chen P, et al. Nanoparticle distribution during systemic inflammation is size-dependent and organ-specific. Nanoscale. 2015;7(38):15863–72. https://doi.org/10.1039/C5NR03626G.
7. Muzzio M, Li J, Yin Z, Delahunty IM, Xie J, Sun S. Monodisperse nanoparticles for catalysis and nanomedicine. Nanoscale. 2019;11(41):18946–67. https://doi.org/10.1039/C9NR06080D.
8. Dheyab MA, Aziz AA, Moradi Khaniabadi P, Jameel MS, Oladzadabbasabadi N, Mohammed SA, et al. Monodisperse gold nanoparticles: a review on synthesis and their application in modern medicine. Int J Mol Sci. 2022;23(13):7400. https://doi.org/10.3390/ijms23137400.
9. Kus-Liśkiewicz MA-O, Fickers PA-O, Ben Tahar I. Biocompatibility and cytotoxicity of gold nanoparticles: recent advances in methodologies and regulations. Int J Mol Sci. 2021;22 (20)(1422–0067). https://doi.org/10.3390/ijms222010952.
10. Yang W, Wang L, Fang M, Sheth V, Zhang Y, Holden AM, et al. Nanoparticle surface engineering with heparosan polysaccharide reduces serum protein adsorption and enhances cellular uptake. Nano Lett. 2022;22(5):2103–11. https://doi.org/10.1021/acs.nanolett.2c00349.
11. Yang W, Frickenstein AN, Sheth V, Holden A, Mettenbrink EM, Wang L, et al. Controlling nanoparticle uptake in innate immune cells with heparosan polysaccharides. Nano Lett. 2022;22(17):7119–28. https://doi.org/10.1021/acs.nanolett.2c02226.
12. Wilhelm S, Bensen RC, Kothapalli NR, Burgett AWGM, R, Stephan C. Quantification of gold nanoparticle uptake into cancer cells using single cell ICP-MS. PerkinElmer Appl Note. 2018. https://resources.perkinelmer.com/lab-solutions/resources/docs/app_014276_01_nexion_sc-icp-ms_np_uptake_in_cancer_cells.pdf. Accessed 15 Nov 2022.
13. Turnbull T, Thierry B, Kempson I. A quantitative study of intercellular heterogeneity in gold nanoparticle uptake across multiple cell lines. Anal Bioanal Chem. 2019;411(28):7529–38. https://doi.org/10.1007/s00216-019-02154-w.
14. Carabineiro SAC. Applications of gold nanoparticles in nanomedicine: recent advances in vaccines. Molecules. 2017;22 (5)(1420–3049). https://doi.org/10.3390/molecules22050857.
15. Elumalai M, Ipatov A, Carvalho J, Guerreiro J, Prado M. Dual colorimetric strategy for specific DNA detection by nicking endonuclease-assisted gold nanoparticle signal amplification. Anal Bioanal Chem. 2022;414(18):5239–53. https://doi.org/10.1007/s00216-021-03564-5.
16. Sánchez-Visedo A, Ferrero FJ, Costa-Fernández JM, Fernández-Argüelles MT. Inorganic nanoparticles coupled to nucleic acid enzymes as analytical signal amplification tools. Anal Bioanal Chem. 2022;414(18):5201–15. https://doi.org/10.1007/s00216-022-03998-5.
17. Modena MM, Rühle B, Burg TP, Wuttke S. Nanoparticle characterization: what to measure? Adv Mater. 2019;31(32):1901556. https://doi.org/10.1002/adma.201901556.
18. Hoo CM, Starostin N, West P, Mecartney ML. A comparison of atomic force microscopy (AFM) and dynamic light scattering (DLS) methods to characterize nanoparticle size distributions. J Nanopart Res. 2008;10(1):89–96. https://doi.org/10.1007/s11051-008-9435-7.
19. Dastanpour R, Boone JM, Rogak SN. Automated primary particle sizing of nanoparticle aggregates by TEM image analysis. Powder Technol. 2016;295:218–24. https://doi.org/10.1016/j.powtec.2016.03.027.
20. Mozhayeva D, Engelhard C. A critical review of single particle inductively coupled plasma mass spectrometry – a step towards an ideal method for nanomaterial characterization. J Anal At Spectrom. 2020;35(9):1740–83. https://doi.org/10.1039/C9JA00206E.
21. Montaño MD, Lowry GV, von der Kammer F, Blue J, Ranville JF. Current status and future direction for examining engineered nanoparticles in natural systems. Environ Chem. 2014;11(4):351–66. https://doi.org/10.1071/EN14037.
22. Bocca B, Battistini B, Petrucci F. Silver and gold nanoparticles characterization by SP-ICP-MS and AF4-FFF-MALS-UV-ICP-MS in human samples used for biomonitoring. Talanta. 2020;220:121404. https://doi.org/10.1016/j.talanta.2020.121404.
23. Xing Y, Han J, Wu X, Pierce DT, Zhao JX. Aggregation-based determination of mercury(II) using DNA-modified single gold nanoparticle, T-Hg(II)-T interaction, and single-particle ICP-MS. Microchim Acta. 2019;187(1):56. https://doi.org/10.1007/s00604-019-4057-6.
24. Xu X, Chen J, Li B, Tang L, Jiang J. Single particle ICP-MS-based absolute and relative quantification of E. coli O157 16S rRNA using sandwich hybridization capture. Analyst. 2019;144(5):1725–30. https://doi.org/10.1039/C8AN02063A.

25. Hu J, Deng D, Liu R, Lv Y. Single nanoparticle analysis by ICPMS: a potential tool for bioassay. J Anal At Spectrom. 2018;33(1):57–67. https://doi.org/10.1039/C7JA00235A.
26. Donahue ND, Kanapilly S, Stephan C, Marlin MC, Francek ER, Haddad M, et al. Quantifying chemical composition and reaction kinetics of individual colloidally dispersed nanoparticles. Nano Lett. 2022;22(1):294–301. https://doi.org/10.1021/acs.nanolett.1c03752.
27. Donahue ND, Francek ER, Kiyotake E, Thomas EE, Yang W, Wang L, et al. Assessing nanoparticle colloidal stability with single-particle inductively coupled plasma mass spectrometry (SP-ICP-MS). Anal Bioanal Chem. 2020;412(22):5205–16. https://doi.org/10.1007/s00216-020-02783-6.
28. Perrault SD, Chan WCW. Synthesis and surface modification of highly monodispersed, spherical gold nanoparticles of 50–200 nm. J Am Chem Soc. 2009;131(47):17042–3. https://doi.org/10.1021/ja907069u.
29. Zheng Y, Zhong X, Li Z, Xia Y. Successive, seed-mediated growth for the synthesis of single-crystal gold nanospheres with uniform diameters controlled in the range of 5–150 nm. Part Part Syst Charact. 2014;31(2):266–73. https://doi.org/10.1002/ppsc.201300256.
30. Liu N, Zhang H, Zhao J, Xu Y, Ge F. Mechanisms of cetyltrimethyl ammonium chloride-induced toxicity to photosystem II oxygen evolution complex of Chlorella vulgaris F1068. J Hazard Mater. 2020;383:121063. https://doi.org/10.1016/j.jhazmat.2019.121063.
31. Tang M, Zhang P, Liu J, Long Y, Cheng Y, Zheng H. Cetyltrimethylammonium chloride-loaded mesoporous silica nanoparticles as a mitochondrion-targeting agent for tumor therapy. RSC Adv. 2020;10(29):17050–7. https://doi.org/10.1039/D0RA02023.
32. Turkevich J, Stevenson PC, Hillier J. A study of the nucleation and growth processes in the synthesis of colloidal gold. Discuss Faraday Soc. 1951;11:55–75. https://doi.org/10.1039/DF9511100055.
33. Schulz F, Pavelka O, Lehmkühler F, Westermeier F, Okamura Y, Mueller NS, et al. Structural order in plasmonic superlattices. Nat Commun. 2020;11(1):3821. https://doi.org/10.1038/s41467-020-17632-4.
34. Zheng Y, Ma Y, Zeng J, Zhong X, Jin M, Li Z-Y, et al. Seed-mediated synthesis of single-crystal gold nanospheres with controlled diameters in the range 5–30 nm and their self-assembly upon dilution. Chem - Asian J. 2013;8(4):792–9. https://doi.org/10.1002/asia.201201105.
35. Pace HE, Rogers NJ, Jarolimek C, Coleman VA, Higgins CP, Ranville JF. Determining transport efficiency for the purpose of counting and sizing nanoparticles via single particle inductively coupled plasma mass spectrometry. Anal Chem. 2011;83(24):9361–9. https://doi.org/10.1021/ac201952t.
36. Pace HE, Rogers NJ, Jarolimek C, Coleman VA, Gray EP, Higgins CP, et al. Single particle inductively coupled plasma-mass spectrometry: a performance evaluation and method comparison in the determination of nanoparticle size. Environ Sci Technol. 2012;46(22):12272–80. https://doi.org/10.1021/es301787d.
37. Laborda F, Bolea E, Jiménez-Lamana J. Single particle inductively coupled plasma mass spectrometry: a powerful tool for nanoanalysis. Anal Chem. 2014;86(5):2270–8. https://doi.org/10.1021/ac402980q.
38. Lee JC, Donahue ND, Mao AS, Karim A, Komarneni M, Thomas EE, et al. Exploring maleimide-based nanoparticle surface engineering to control cellular interactions. ACS Appl Nano Mater. 2020;3(3):2421–9. https://doi.org/10.1021/acsanm.9b02541.
39. Li J, Zhu B, Zhu Z, Zhang Y, Yao X, Tu S, et al. Simple and rapid functionalization of gold nanorods with oligonucleotides using an mPEG-SH/Tween 20-assisted approach. Langmuir. 2015;31(28):7869–76. https://doi.org/10.1021/acs.langmuir.5b01680.
40. Slesiona N, Thamm S, Stolle HLKS, Weißenborn V, Müller P, Csáki A, et al. DNA-biofunctionalization of CTAC-capped gold nanocubes Nanomaterials. 2020;10(6):1119. https://doi.org/10.3390/nano10061119.
41. Lee C-Y, Nguyen P-CT, Grainger DW, Gamble LJ, Castner DG. Structure and DNA hybridization properties of mixed nucleic acid/maleimide−ethylene glycol monolayers. Anal Chem. 2007;79(12):4390–400. https://doi.org/10.1021/ac0703395.
42. Chou LYT, Zagorovsky K, Chan WCW. DNA assembly of nanoparticle superstructures for controlled biological delivery and elimination. Nat Nanotechnol. 2014;9(2):148–55. https://doi.org/10.1038/nnano.2013.309.
43. Zagorovsky K, Chou LYT, Chan WCW. Controlling DNA–nanoparticle serum interactions. Proc Natl Acad Sci. 2016;113(48):13600–5. https://doi.org/10.1073/pnas.1610028113.
44. Maguire CA-O, Rösslein M, Wick P, Prina-Mello AA-O. Characterisation of particles in solution - a perspective on light scattering and comparative technologies. Sci Technol Adv Mater. 2018;19 (1)(1468–6996):732–45. https://doi.org/10.1080/14686996.2018.1517587.
45. Khlebtsov NG. Determination of size and concentration of gold nanoparticles from extinction spectra. Anal Chem. 2008;80(17):6620–5. https://doi.org/10.1021/ac800834n.
46. Shafiqa AR, Abdul Aziz A, Mehrdel B. Nanoparticle optical properties: size dependence of a single gold spherical nanoparticle. J Phys: Conf Ser. 2018;1083(1):012040. https://doi.org/10.1088/1742-6596/1083/1/012040.
47. Huang Y, Kim D-H. Synthesis and self-assembly of highly monodispersed quasispherical gold nanoparticles. Langmuir. 2011;27(22):13861–7. https://doi.org/10.1021/la203143k.
48. Lee S, Bi X, Reed RB, Ranville JF, Herckes P, Westerhoff P. Nanoparticle size detection limits by single particle ICP-MS for 40 elements. Environ Sci Technol. 2014;48(17):10291–300. https://doi.org/10.1021/es502422v.
49. Suk JS, Xu Q, Kim N, Hanes J, Ensign LM. PEGylation as a strategy for improving nanoparticle-based drug and gene delivery. Adv Drug Delivery Rev. 2016;99 (A)(1872–8294):28–51. https://doi.org/10.1016/j.addr.2015.09.012.
50. Jokerst JV, Lobovkina T Fau - Zare RN, Zare Rn Fau - Gambhir SS, Gambhir SS. Nanoparticle PEGylation for imaging and therapy. Nanomedicine. 2011;6 (4)(1748–6963). https://doi.org/10.2217/nnm.11.19.
51. Kokkin DL, Zhang R, Steimle TC, Wyse IA, Pearlman BW, Varberg TD. Au–S bonding revealed from the characterization of diatomic gold sulfide. AuS J Phys Chem A. 2015;119(48):11659–67. https://doi.org/10.1021/acs.jpca.5b08781.
52. Bürgi T. Properties of the gold–sulphur interface: from self-assembled monolayers to clusters. Nanoscale. 2015;7(38):15553–67. https://doi.org/10.1039/C5NR03497C.
53. Dai Q, Wilhelm S, Ding D, Syed AM, Sindhwani S, Zhang Y, et al. Quantifying the ligand-coated nanoparticle delivery to cancer cells in solid tumors. ACS Nano. 2018;12(8):8423–35. https://doi.org/10.1021/acsnano.8b03900.
54. Syed AM, Sindhwani S, Wilhelm S, Kingston BR, Lee DSW, Gommerman JL, et al. Three-dimensional imaging of transparent tissues via metal nanoparticle labeling. J Am Chem Soc. 2017;139(29):9961–71. https://doi.org/10.1021/jacs.7b04022.
55. Wang F, Chen B, Yan B, Yin Y, Hu L, Liang Y, et al. Scattered Light imaging enables real-time monitoring of label-free nanoparticles and fluorescent biomolecules in live cells. J Am Chem Soc. 2019;141(36):14043–7. https://doi.org/10.1021/jacs.9b05894.